Impacts of Altitude on Expectation Maximization-based Data Association and Orbit Estimation

Georgia Tech Space Systems Design Laboratory
School of Aerospace Engineering

AE 8900 MS Special Problems Report

Space Systems Design Lab (SSDL)
Daniel Guggenheim School of Aerospace Engineering
Georgia Institute of Technology, Atlanta, GA

Author:
Daniel Sakson

Advisor:
Dr. Brian C. Gunter

August 6, 2022

Impacts of Altitude on Expectation Maximization-based Data Association and Orbit Estimation

Daniel Sakson*
Georgia Institute of Technology, Atlanta, GA, 30332

Given the current number of resident space objects (RSO) and growing concerns over space debris and collisions, efficient methods of multiple target tracking and data association are required. The robustness of an expectation maximization (EM) based technique proposed by Bernstein was evaluated for its suitability to meet this need. A model was developed to simulate optical measurements from a space-based observer to multiple RSOs in various orbits. These measurements were used in the proposed algorithm to estimate data association probabilities and orbital states. In the process of validating the algorithm implementation it was found that the orbital estimates did not converge to expected levels; However, the algorithm's classification exceeded an adjusted Rand index (ARI) and Rand index (RI) of 90% indicating good performance. The estimation and classification performance were considered decoupled and a study was then performed to understand the affects of various observer-object geometries on the algorithm's classification ability. Objects were placed into orbits of varying altitudes in two observer configurations. It was found that algorithm performance was positively correlated to object altitude. Further analysis found an additional correlation between performance and the measurement-to-clutter ratio (MCR). When this ratio exceeds a value of 5, performance in excess of 80% ARI and 90% RI can be attained. Two linear models were build to predict the Rand indices as a function of the CMR. The study was concluded with a discussion of potential future improvements to the simulation and estimation scheme including higher order dynamics and sensor models.

I. Nomenclature

z	=	altitude
ζ	=	states estimates in expectation maximization
λ	=	spherical normal measurement concentration
Θ	=	object initial orbital states
π	=	mixing proportions for expectation maximization
r	=	position
$\dot{r}$	=	velocity
E_λ	=	absolute concentration error
$E_{\Theta,r}$	=	mean position error
$E_{\Theta,\dot{r}}$	=	mean velocity error
E_π	=	norm of mixing proportion error
R	=	Rand index
R_A	=	adjusted Rand index
MCR	=	measurement-to-clutter ratio
ρ_y	=	measurement concentration
N	=	number of measurements
θ	=	measured azimuth
ϕ	=	measured elevation
$\tilde{r}$	=	observer to object pointing vector
C	=	spherical normal normalization parameter
t	=	time

*Graduate Student - Daniel Guggenheim School of Aerospace Engineering

Y	=	set of all available measurements
y_i	=	measurement at time t_i
w	=	mixing weights for expectation maximization
Q	=	mixing model complete-data log-likelihood function
μ	=	Earth's gravitation parameter
h	=	EM iteration
l	=	mixing model marginal log-likelihood function

II. Introduction

The challenge of detecting and tracking resident space objects (RSO) has been a topic of interest for a large part of the 21st century [1]. Particularly of interest is simultaneous tracking of multiple objects. This interest is spurned by the rise in the number of large satellite constellations [2] and concerns over the impacts of debris on operational satellites and constellations [3]. Multiple object tracking is a mature field, but the rate of increase in the number of RSOs is quickly outpacing the ability of existing techniques [4]. This calls to attention the need for new techniques that can be leveraged across a number of sensing platforms and/or networks of these platforms to associate large quantities of measurements and estimate precise RSO orbits.

A recently developed technique that falls in line with this need is the application of expectation-maximization (EM) to the data association and orbit determination problem. In general, expectation-maximization, aims to iteratively determine a maximum likelihood estimate (MLE) from incomplete data [5]. This technique has been applied a number of times to the data association and orbit determination problem [6–10], and was recently refined by Bernstein through the proposal of two EM-based algorithms [11].

Bernstein's algorithms provide methods that address multiple challenges in this space. First, they are able to classify measurements not just among multiple tracked objects, but also measurements originating from various types of clutter. Second, in using a model of the objects dynamics, they are able to provide a MLE for each objects initial orbital state. Lastly, the techniques are data agnostic. The initial work was done with generalized optical angle measurements, but the technique could be extended to any number of sensor configurations so long as a pointing vector can be determined.

The first of these algorithms, a single-stage EM approach, falls in line with traditional mixture models such as the Guassian Mixture Model [12]. It aims to provide an MLE of the orbit states, X, the measurement concentration, λ, and the mixing proportions, π, between the objects and clutter. A key assumption of this method is the apriori knowledge of the number of orbits to be fit to the data. The second algorithm, a multi-stage EM approach, does away with the need for this apriori knowledge by extended the single-stage approach with additional iterations while removing successfully associated measurements. Both algorithms are described in detail in [11].

Although promising, these EM based approaches are not without potential challenges. The techniques were validated against an observer and objects in mid-Earth orbit (MEO). In this region dynamics are slow between the observer and objects by nature of the slower orbital velocities in this region. This provides the EM technique consistent data from all objects under track and, periodically, clutter. In lower-altitude scenarios the clutter-to-measurement ratio may skew greatly towards clutter. Additional challenges may stem from the lack of higher-order dynamics in the orbit model. These dynamics, especially atmospheric drag and non-spherical earth effects, add to the computational complexity associated with propagating the orbital state forward in time. When added to the iterative nature of EM, and the large number of possible objects and measurements, the computational complexity of this technique may make it unfavorable compared to existing methodologies.

The goal of this work is to assess the impacts of the orbital altitude single-stage EM methodology. Impact on errors from the validation performed in [11] will be assessed as well as association performance. If possible, regions of expected performance will be defined and reasons for degraded performance discussed.

III. Methodology

Both the single-stage and multi-stage EM implementations are described in detail in [11]. For completeness, and to highlight key differences in implementation, a summary of the single-stage algorithm is presented in Section III.A. Once implemented and validated, testing will focus on two key orbital altitude regions: low-earth orbit (LEO) and mid-Earth orbit (MEO). The observer and objects will be initialized in these regions and measurements collected and processed through Algorithm 1. Selected test points are summarized in Table 1.

These points were chosen to provide variable resolutions in the regions of interest. Five points were placed linearly between 150km and 2000km altitude. This provides a resolution of 462.5 km in this region. In MEO, five points are also linearly spaced between the LEO boundary at 2000 km and 13621.9 km. One of these points overlaps with a LEO test points resulting in four total MEO points with an altitude resolution of 2905.5 km.

Point	z_{obs} (km)	z_{obj} (km)	Point	z_{obs} (km)	z_{obj} (km)
1	13621.9	150	10	1000	150
2	13621.9	612.5	11	1000	612.5
3	13621.9	1075	12	1000	1075
4	13621.9	1537.5	13	1000	1537.5
5	13621.9	2000	14	1000	2000
6	13621.9	4905.5	15	1000	4905.5
7	13621.9	7810.9	16	1000	7810.9
8	13621.9	10716.4	17	1000	10716.4
9	13621.9	13621.9	18	1000	13621.9

Table 1 Test Points

Results will be evaluated separately for estimation and classification performance. To do so several key values must be defined. First is the list of parameters to be estimated.

$$\hat{\zeta} = \left[\hat{\lambda}, \hat{\Theta}, \hat{\pi}\right] \tag{1}$$

In this set we see the concentration, $\hat{\lambda}$, the initial orbital state estimates, $\hat{\Theta}$, and the mixing proportions, $\hat{\pi}$. Both $\hat{\Theta}$ and $\hat{\pi}$ are matrices or vectors in their own right.

$$\begin{aligned} \hat{\Theta} &= \begin{bmatrix} \hat{\Theta}_r & \hat{\Theta}_{\dot{r}} \end{bmatrix} \\ &= \begin{bmatrix} \hat{r}_{x,1} & \hat{r}_{y,1} & \hat{r}_{z,1} & \hat{\dot{r}}_{x,1} & \hat{\dot{r}}_{y,1} & \hat{\dot{r}}_{z,1} \\ \vdots & \vdots & \vdots & \vdots & \vdots & \vdots \\ \hat{r}_{x,J} & \hat{r}_{y,J} & \hat{r}_{z,J} & \hat{\dot{r}}_{x,J} & \hat{\dot{r}}_{y,J} & \hat{\dot{r}}_{z,J} \end{bmatrix} \end{aligned} \tag{2}$$

$$\hat{\pi} = \begin{bmatrix} \hat{\pi}_0 & \dots & \hat{\pi}_J \end{bmatrix} \tag{3}$$

J here represents the total number of orbits to be estimated. In this investigation J will be set to 4 to match the original work [11]. To assess the impacts of the altitudes imposed by the test points in Table 1, we define error terms for each of the parameters.

$$E_{\lambda} = |\hat{\lambda} - \lambda| \tag{4}$$

$$E_{\Theta_r} = \frac{1}{J} \sum_{j=1}^{J} ||\hat{\Theta}_{r,j} - \Theta_{r,j}||_2^2 \tag{5}$$

$$E_{\Theta_{\dot{r}}} = \frac{1}{J} \sum_{j=1}^{J} ||\hat{\Theta}_{\dot{r},j} - \Theta_{\dot{r},j}||_2^2 \tag{6}$$

$$E_{\pi} = ||\hat{\pi} - \pi||_2^2 \tag{7}$$

Listed in order here are the concentration error, mean position error, mean velocity error, and the mixing proportion error. These will be plotted with respect to the altitude of the objects, z_{obj}. This analysis will show how effective the algorithm is in estimation at each altitude of interest.

Additionally the algorithms are analyzed in their classification through the Rand and adjusted Rand indices [13, 14]. These metrics assess how measurements are labeled by the algorithm compared to the true labels for said measurement. The difference between these two metrics can be seen by analyzing their formulations.

$$R = \frac{a+b}{\binom{n}{2}} \tag{8}$$

$$R_A = \frac{\sum_{ij}\binom{n_{ij}}{2} - \left[\sum_i \binom{a_i}{2}\sum_j \binom{b_j}{2}\right]\Big/\binom{n}{2}}{\frac{1}{2}\left[\sum_i \binom{a_i}{2} + \sum_j \binom{b_j}{2}\right] - \left[\sum_i \binom{a_i}{2}\sum_j \binom{b_j}{2}\right]\Big/\binom{n}{2}} \tag{9}$$

Both are based on the contingency matrix. This matrix represents how the true labels compare to those predicted by a classification algorithm [15]. n represents the total number of labels while n_{ij} is the individual overlap between the group labeled as X_i and the true label Y_j. Then a is the sum of all overlaps in the predicted direction, and b the sum in the true direction. With this we see that the ARI is adjusted to account for the baseline similarity in the data through possible permutations. This allows the ARI to better score dissimilar groupings as would be the case if a different number of labels are predicted from truth. This change makes the algorithm more robust for the possible inclusion of multi-stage EM where the number of labels is an estimated quantity rather than pre-determined.

In addition to analyzing the results of the algorithm and the associated errors, the generated measurements will be analyzed to gain insight into phenomena potentially affecting the estimation scheme. The first focus will be the proportion of measurements to the clutter in the true set of labels. To assess this we define a new quantity, the measurement-to-clutter ratio (MCR)

$$MCR = \frac{\sum_{i=1}^{N} \begin{cases} 1 & \mathbf{if(y_i \notin J = 0)} \\ 0 & \mathbf{otherwise} \end{cases}}{\sum_{i=1}^{N} \begin{cases} 1 & \mathbf{if(y_i \in J = 0)} \\ 0 & \mathbf{otherwise} \end{cases}} \tag{10}$$

This defines the ratio between measurements and clutter in a formulation similar to a signal-to-noise ratio (SNR) used in traditional astronomical sensing [16]. This metric will assist in identifying impacts caused by increased (or reduced) object occlusion due to Earth. Since a reduction in the number of measurements classified as objects also implies fewer measurements it is possible that a low MCR could degrade algorithm performance.

The final metric to be considered is the elevation range of the measurements, and moreover the density of measurements. Elevation is strictly a function of the observer-object geometry. Objects at lower altitudes will be dispersed across a smaller range of elevations and vise-versa for observers at higher altitudes. We can then define the measurement density as the number of measurements normalized by the solid angle [17] formed by the azimuth and elevation ranges.

$$\rho_y = \frac{N}{(\theta_{max} - \theta_{min})(\sin(\phi_{max}) - \sin(\phi_{min}))} \tag{11}$$

Classification and estimation performance will be assessed against both of these metrics to quantify and correlation and identify any possible causation between them.

A. Single-Stage EM

The single-stage EM methodology leverages directional statistics in combination with the general EM methodology. The algorithm is initialized with the assumption that equal proportions of each object and clutter exist. Then, the EM iterations begin. During the expectation step (E-Step) the current estimates of the object states are leveraged to calculate the pointing vector from the observer to each object as:

$$\tilde{r}(t, X) = r(t, X) - r_O(t) \tag{12}$$

Where $r(t, X)$ is the position of a particular object at time t and $r_O(t)$ is the corresponding position of the observer. It is assumed that the position of the observer is perfectly known in this formulation and thus is not part of the estimation scheme. Next, the pointing information, along with the current estimate of the measurement concentration, is used to parameterize a spherical normal [18], conditional probability density function .

$$p(y_i|X_i = j) = [C(\lambda)]^{-1} \exp\left(-\frac{\lambda}{2} \arccos^2 \left(\frac{y_i^T \tilde{r}(t; X_j)}{||\tilde{r}(t; X_j)||} \right) \right) \tag{13}$$

In this equation $C(\lambda)$ is the normalization term for the conditional probability. The function $C(\lambda)$ is non-linear and defined in further detail in the supplement to [18]. This value was approximated (14) in the referenced work due to the difficulty in solving the function through maximization.

$$C(\lambda) \approx \frac{2\pi}{\lambda} \tag{14}$$

Also in Equation (13), we have the angle measurements y_i. These are represented as a unit Cartesian pointing vector. Measurements are generated according to the methodology laid out in the supplement to [11]. Orbits are propagated for 6 days and measurements sampled every ten minutes during that period. A random object is sampled at each time-step. If said object is occluded by Earth, as defined by Vallado [19], clutter is sampled instead from a uniform spherical distribution.

$$p(y_i|X_i = 0) = (4\pi)^{-1} \tag{15}$$

When not occluded, the objects are sampled from the spherical normal distribution [18] treating the pointing vector as the mean vector and setting the concentration parameter, $\lambda = 10^7$. Labels for each measurement are recorded such that clutter is assigned a label of 0 and objects are labeled from 1 to J depending on the quantity.

With this information, the mixing weights are calculated for each measurement and each orbit estimate. These define the association probabilities between each measurement and each object (or clutter).

$$w_{ij} = \frac{p(y_i|X_i = j)\pi_j}{\sum_{j=0}^{J} p(y_i|X_i = j)\pi_j} \tag{16}$$

Once the mixing weights are computed the E-Step is complete and the maximization step (M-Step) begins. In the M-Step, parameter estimates are updated either in closed form or by maximizing the complete-data log-likelihood (CDLL) function. A closed form update for the mixing proportion is possible through the column-wise mean of the mixing weights.

$$\pi_j = \sum_{i=1}^{N} w_{ij} \tag{17}$$

The orbital state estimate and the concentration estimate cannot be updated in closed form. For these parameters, an optimization scheme is employed to maximize the CDLL function.

$$Q(\zeta, \zeta^{(h-1)}) = \sum_{i=1}^{N} \sum_{j=0}^{J} [\log(p(y_i|X_i = j)) + \log(\pi_j)] w_{ij}^{(h-1)} \tag{18}$$

In this formulation ζ represents the parameters being estimated (e.g. $\zeta = [\lambda, X, \pi]$). Although not complex in appearance, this optimization is made non-trivial by the $p(y_i|X_i = j)$ term's dependence on being able to calculate the position of each object at each measurement time. This is complex computationally as these positions must be recomputed on each evaluation of the CDLL. In this CDLL are also the first deviations from the original algorithm as proposed in the referenced work.

Unlike the referenced work the Earth-centered inertial (ECI) position, r, and velocity, $\dot{r}$, are used to parameterize the orbit. These are used in a numerical integration scheme to compute the position and velocity of the orbit at all measurement times. A Runge-Kutta 4 based integrator [20] is used to integrate the time derivative of the state vector.

$$\begin{aligned} X &= \left[r, \dot{r} \right]^T \\ &= \left[r_x, r_y, r_z, \dot{r}_x, \dot{r}_y, \dot{r}_z \right]^T \end{aligned} \tag{19}$$

$$
\begin{aligned}
\frac{dX}{dt} &= \frac{d}{dt}\left[r, \dot{r}\right]^T \\
&= \left[\dot{r}_x, \dot{r}_y, \dot{r}_z, -\frac{\mu}{||r||} r_x, -\frac{\mu}{||r||} r_y, -\frac{\mu}{||r||} r_z\right]^T
\end{aligned}
\tag{20}
$$

This is in contrast to the formulation used in [11]. There, the equinoctical orbital elements [21] were used to parameterize the orbit which was propagated through solving Kepler's equation. The smaller number of state variables in the equinoctical representation allow for a smaller number of objective function evaluations during optimization. However using the position and velocity, as noted by the author, allows for the introduction of higher order dynamics. Although higher order dynamics were not introduced in this work, Cartesian state representation was used to facilitate future growth.

The final difference between this implementation and the original algorithm is the optimizer. The referenced work utilized a Lavenberg-Marqardt [22] weighted least squared formulation to obtain estimates of the state. Lavenberg-Marqardt is well suited for this problem, but not implemented widely in common toolsets. A different, Quasi-Newton-based, solver [23] was used for this work. This difference adds complexity to validating the original algorithm as two dissimilar optimizers are unlikely to return similar state estimates. These differences and their impact on the results are discussed in subsequent sections. Regardless of solver, the following problem was solved.

$$
\zeta_h = \max_{\zeta} \sum_{i=1}^{n} \sum_{j=0}^{J} w_{ij}^{(h-1)} \left[\log(p_\zeta(Y_i|X_i = j)) + \log(\pi_j)\right] \tag{21}
$$

An important portion of the optimization scheme is the value of λ. Although not immediately evident in equation (21), the conditional probabilitiy term for $j \in [1, J]$ is a function of λ. The concentration itself is a non-linear function [18] that is difficult to obtain through the optimization process alone. For this reason an approximation is used to estimate its value as a function of the current orbital states and the measurements.

$$
\lambda^h \approx \frac{\sum_{i=1}^{N} \sum_{j=1}^{J} w_{ij}^{(h-1)}}{\frac{1}{2} \sum_{i=1}^{N} \sum_{j=1}^{J} \arccos^2\left(\frac{Y_i^T \tilde{r}(t_i, X_j^h)}{||\tilde{r}(t_i, X_j^h)||}\right) w_{ij}^{(h-1)}} \tag{22}
$$

Once the optimization converges on a solution, state variables are compared to their values in the previous iteration for convergence of the EM algorithm. Additionally, the marginal log-likelihood function is evaluated and compared to its value in the previous iteration.

$$
l_Y(\zeta) = \sum_{i=1}^{N} \log\left(\sum_{j=0}^{J} p(y_i|X_i = j)\pi_j\right) \tag{23}
$$

Algorithm 1 provides an overview along with specifics on stopping criteria used in data gathering and model validation.

Algorithm 1 Single-Stage Expectation Maximization

$h \leftarrow 1$
$X_{(h-1)} \leftarrow X_0$
$\lambda_{(h-1)} \leftarrow \lambda_0$
$l_{(h-1)} \leftarrow 999999$
$\pi_j \leftarrow (J+1)^{-1} \forall J$
while $h \leq 25$ and $(|l_h - l_{(h-1)}| \geq 10^{-8}$ or $||\zeta_h - \zeta_{(h-1)}|| \geq 10^{-8})$ **do**
  $w_{ij}^{(h-1)} \leftarrow \frac{p(y_i|X_i=j)\pi_j}{\sum_{j=0}^{J} p(y_i|X_i=j)\pi_j}$ ▷ E-Step
  $pi_j^h \leftarrow \sum_{i=1}^{N} w_{ij}$ ▷ BEGIN: M-Step
  $\zeta^h \leftarrow \min_\zeta \sum_{i=1}^{n} \sum_{j=0}^{J} -w_{ij}^{(h-1)} [\log(p_\zeta(Y_i|X_i=j)) + \log(\pi_j)]$ ▷ END: M-Step
  $l^h \leftarrow \sum_{i=1}^{N} \log\left(\sum_{j=0}^{J} p(y_i|X_i=j)\pi_j\right)$
  $h \leftarrow h+1$
end while

B. Model Validation

To validate the algorithm, results were compared to the original work. The object and observer orbits are detailed in the supplement to [11] as sets of classical elements. The estimation errors along with classification metrics are compared to those in the original reference in order to claim that recreated algorithm is functioning similarly. Measurements and true orbits generated for validation are plotted for a first stage-comparison the the original implementation.

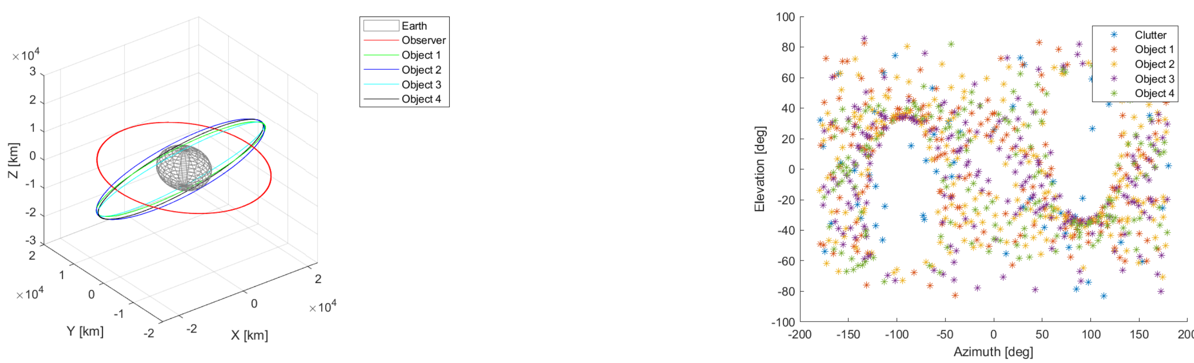

(a) Orbits **(b) Measurements**

Fig. 1 Data generated for algorithm validation

Both sets of generated data are well in family of the original work. Measurements range between ±80 degrees elevation and exhibit the same characteristic sinusoidal patterns. The sinusoidal pattern in the generated measurements is flipped when compared to the original author. This can be attributed to a different starting epoch for the orbits compared to [11]. These measurements were fed into the single-stage EM algorithm and run six times with six different initial orbit estimates to facilitate convergence. An initial concentration estimate of 10^2 was used to initialize the algorithm which matches the tests performed previously. Results are plotted below and highlight the quantities of interest: log-likelihood, position errors, velocity errors, concentration errors, Rand index, accuracy, and clutter false discovery rate.

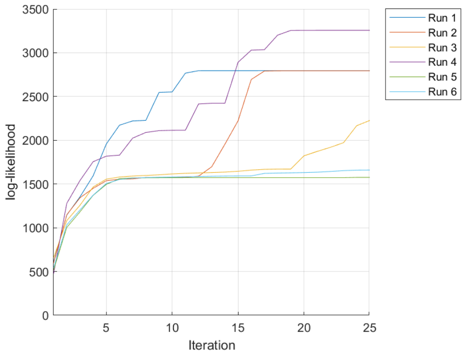

(a) Log-Likelihood

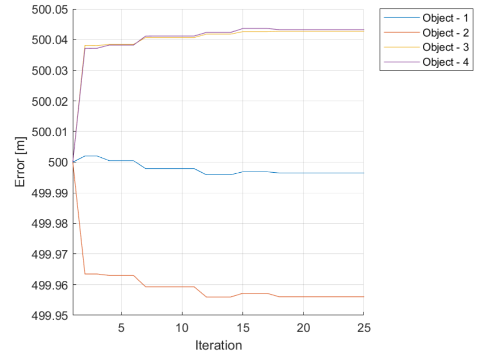

(b) Position Errors - Run 4

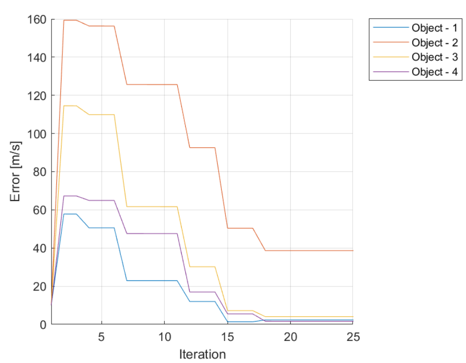

(c) Velocity Errors - Run 4

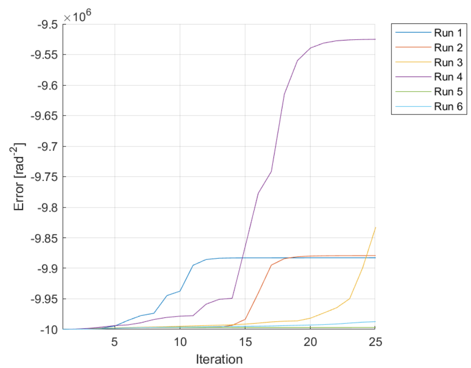

(d) λ Error

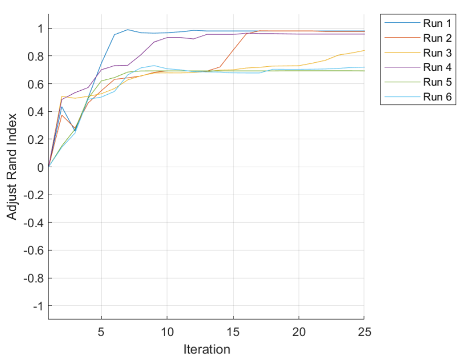

(e) Validation Results - Adjusted Rand Index

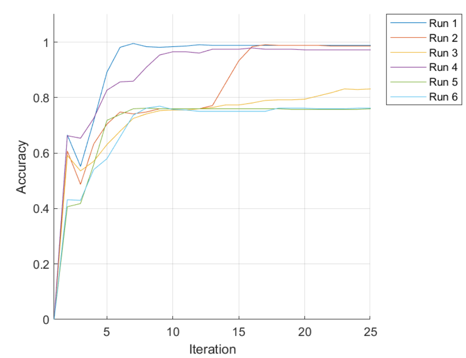

(f) Validation Results - Clutter Detection Accuracy

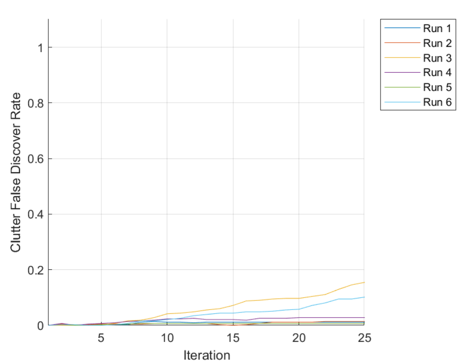

(g) Clutter False Detection Accuracy

Fig. 2 Model Validation

We see that the implemented algorithm converges, but does not do so on a precise initial orbital state. With four objects, there is little change in the position state. The position error remains near 500 m for all objects in all runs. The velocity estimate improves from $10\frac{m}{s}$ of initial error to an average of $3\frac{m}{s}$ of initial error with the exception of the second object which converged to an error of $40\frac{m}{s}$. Although log-likelihood remains in family with the expected results, the estimates of the other parameters do not build confidence that the algorithm is identical to the reference. This is in contrast with how well the algorithm performs as a classifier.

The three measures of classification performance demonstrate that, as a classifier, this implementation of the single-state EM algorithm performs comparable to the original implementation. Both algorithms converge to ARIs and Accuracies over 96% while maintaining low clutter false discovery rates.

These results are mixed for the purposes of validating the correct implementation of the algorithm. This is likely due to the difference in optimizer used in this work. Regardless, it is possible to decouple the two portions of the algorithm. Analyzing the classification, which is shown to be comparable in Figures (2e, 2f, 2g), will be the focus of the subsequent performance evaluation. This is based on the assumption that resolving the issue with the maximization that result in sub-optimal estimation performance would only serve to improve the results of the classification. Therefor any positive results in favor of the single-stage EM algorithm would still stand regardless of the challenges of this particular implementation.

IV. Results

With the model's classification ability validated, measurements were generated according to Table 1. A subset of these measurements are plotted in Figure 3 to visualize different trends at altitude. Each set of measurements contained 433 total points, with varying proportions of measurements and clutter.

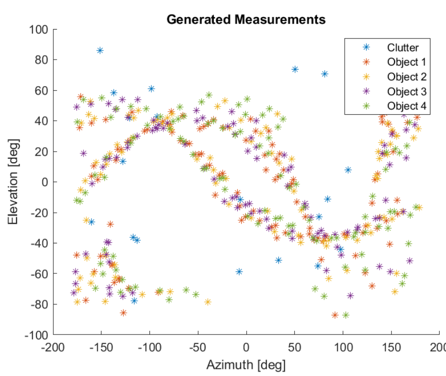

(a) Test Point 1 - Observer 13622 km - Objects 13622 km

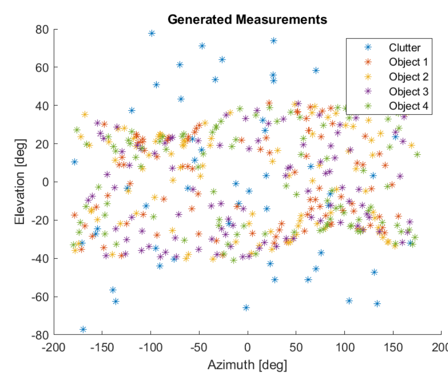

(b) Test Point 9 - Observer 13622 km - Objects 1000 km

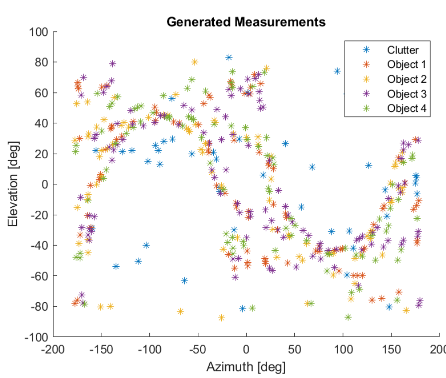

(c) Test Point 10 - Observer 1000 km - Objects 13622 km

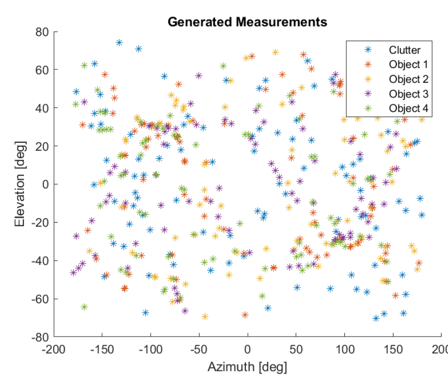

(d) Test Point 18 - Observer 1000 km - Objects 1000 km

Fig. 3 Measurement Examples

In these points we see the measurements vary as a function of the altitudes. High-altitude co-orbital scenarios, Figure 3a, show tightly grouped "streaks" of measurements with clutter scattered throughout the field-of-view. Scenarios with a large altitude difference between the observer depend on observer altitude. When the observer is at a higher altitude than the objects, Figure 3b, we see the measurements are more tightly grouped in elevation. The inverse of this is true when the observer is at a lower altitude with respect to the objects. In that scenario, Figure 3c we see the measurements span a larger range, encompassing nearly the entire ±90 degree field of view. Additionally, in this configuration we again see tighter groupings of measurements similar to those in the high-altitude co-orbital case. The final configuration is an overall low-altitude scenario with relatively close observer and objects. We see here the measurements span the range of ±70 degrees and exhibit fewer defined patterns than other configurations. To further display the impact of the geometry on the measurements we take a look at the true mixing proportions in these same four scenarios.

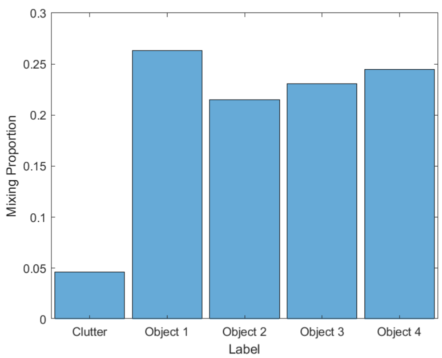

(a) Test Point 1

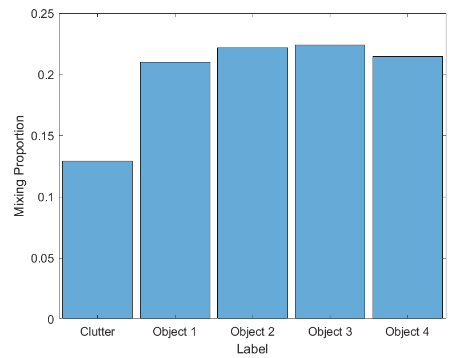

(b) Test Point 9

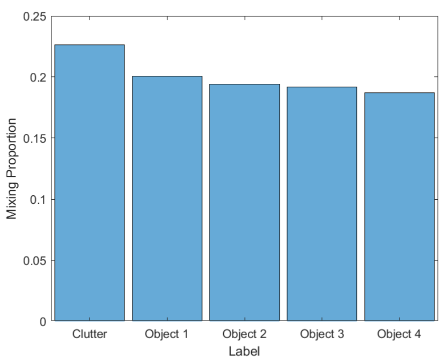

(c) Test Point 10

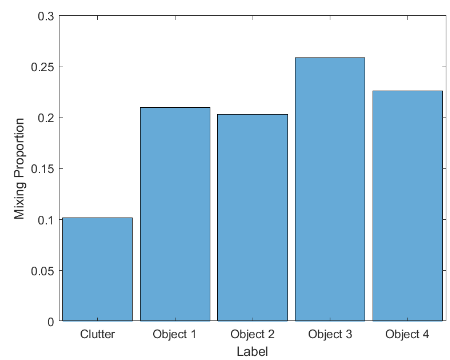

(d) Test Point 18

Fig. 4 True Measurement Mixing Proportions

From the true mixing proportions we see there is a variable proportion of clutter at the different test points. Comparing all points this value ranges from a minimum of 5% to a maximum of 22.5%. This variability in the clutter proportion is further highlighted by plotting the MCR at each object altitude for both observer altitudes along with the measurement density.

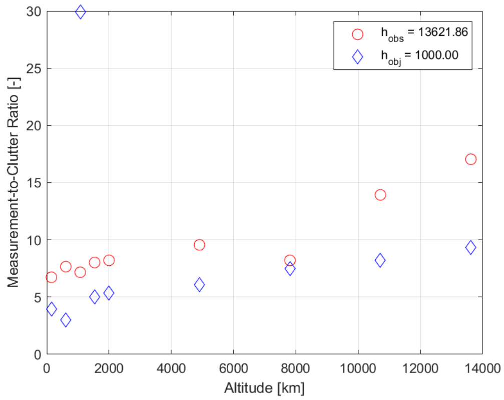

(a) Clutter-to-Measurement ratio per test point

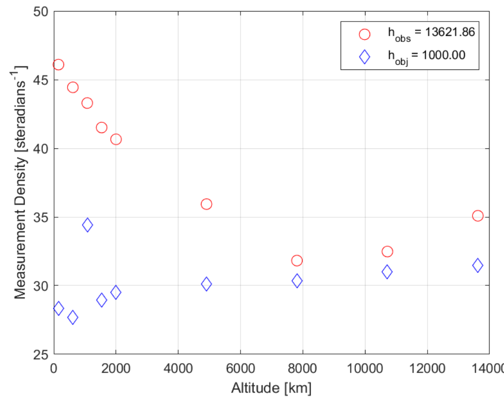

(b) Measurement density per test point

Fig. 5 Measurement properties

Both measurement metrics show impacts from altitude. The MCR is directly correlated to object altitude. As the object altitude increases the MCR grows from a value of 3.97 to 9.31 for the LEO observer and from 6.73 to 17.04 for the MEO observer. Measurement density does not show the same trend. The measurement density for the low altitude observer mirrors the MCR for the same case, but the high-altitude observer shows nearly the reverse trend. As altitude increases the density trends from a value of 46.0941 $steradians^{-1}$ at 150 km to 31.8227 $steradians^{-1}$ at 7810.9 km. Past that point the measurement density begins to increase again to a final value of 35.0863 $steradians^{-1}$ at 13622 km.

Moving on from the measurements themselves, the estimation and classification results of the algorithm were analyzed. Each of the quantities of interest are plotted with respect to altitude. Individual points are averages of ten runs with different initialization.

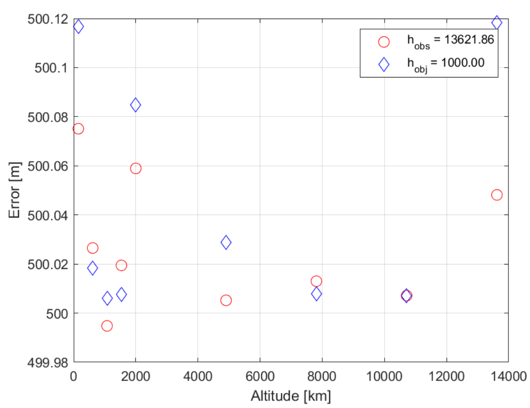

(a) Position

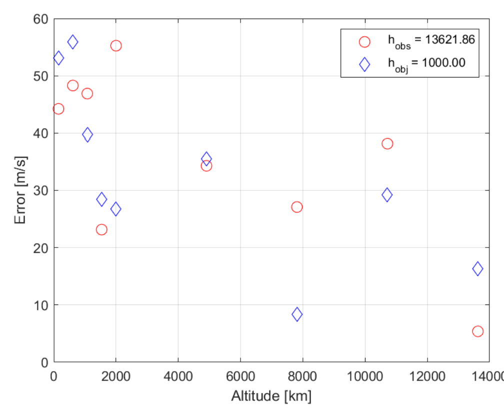

(b) Velocity

Fig. 6 Mean Position and Velocity Errors

As mentioned in the discussion on algorithm validation, position and velocity do not match the level of convergence demonstrated in the original implementation. That being said, we do see a trend in the velocity error. For both observer altitudes, as object altitude increases, the mean velocity error tends to decrease. With the initial error set at ten meters, objects closest to Earth had errors ranging from 44.22 to 53.09 m/s. Meanwhile, objects furthest from earth had errors ranging from just 5.39 to 16.32 m/s. Given the magnitude of the differences observed for the position error, a trend cannot be similarly identified. While reviewing the position and velocity errors it was also import to quantify the other estimated quantities: concentration and mixing proportion.

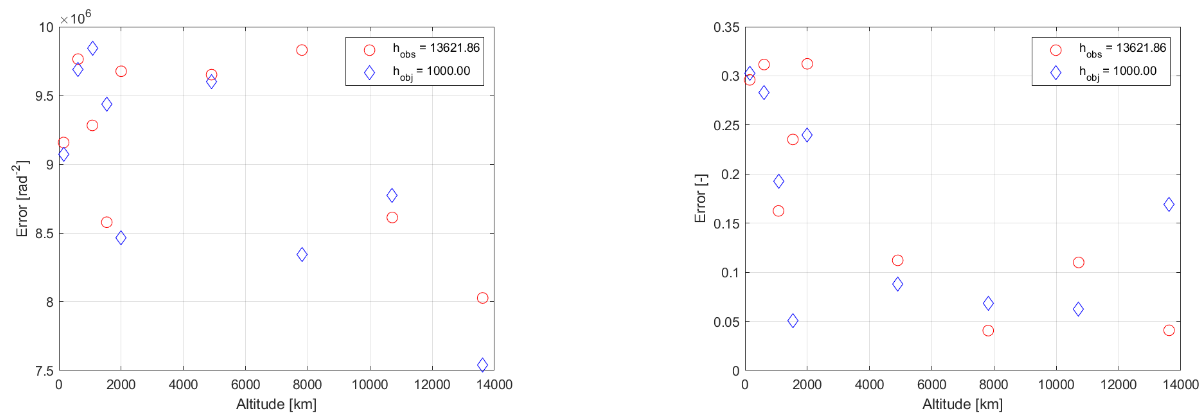

(a) Concentration **(b) Mixing Proportion**

Fig. 7 Mean Concentration and Mixing Errors

Concentration is similarly impacted in this scheme by the issues in algorithm implementation. Although a trend in decreasing error could be argued, there is insufficient confidence in the estimation scheme to support it. On the other hand, as the mixing proportion is independent of the maximization in the EM algorithm we see a trend of decreasing error with increasing altitude. Errors exceed 30% closest to earth and achieve values between 4.09% and 16.9%. This decay appears more stable with higher observer orbits than with the LEO observer. Moving onto classification performance, we continue to see correlation with altitude.

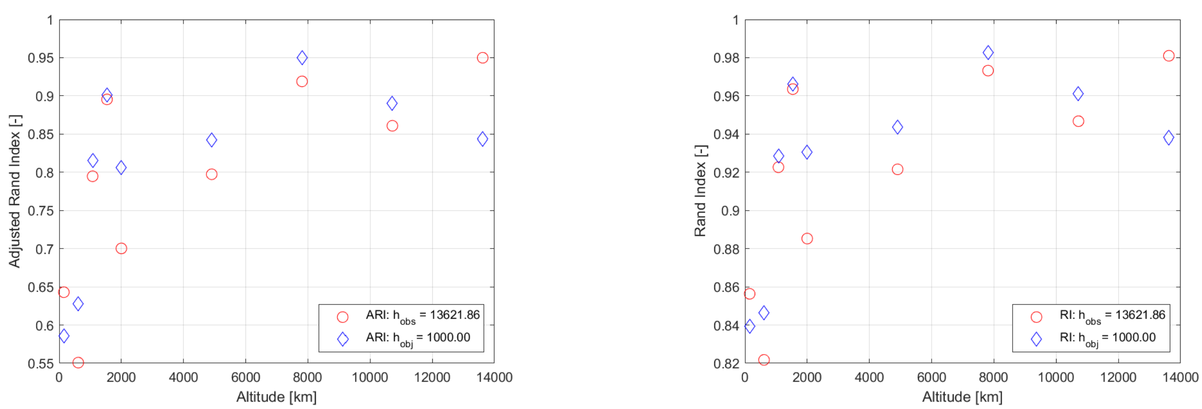

(a) Adjusted Rand Index **(b) Rand Index**

Fig. 8 Rand and Adjusted Rand Indices

Both the Rand and Adjusted Rand indices are plotted. The former is used as a point of comparison to the original work while the adjusted rand to act as a new data point. Both metrics predict good performance at high altitudes and predict degraded performance as altitude decreases. Comparing the relative magnitude of the two indices, we see that the ARI is nearly a shifted version of the RI. Points on both follow the same general patterns but the ARI is lower by over 20% in low altitude regions. This is trend is even clearer if the results are overlaid.

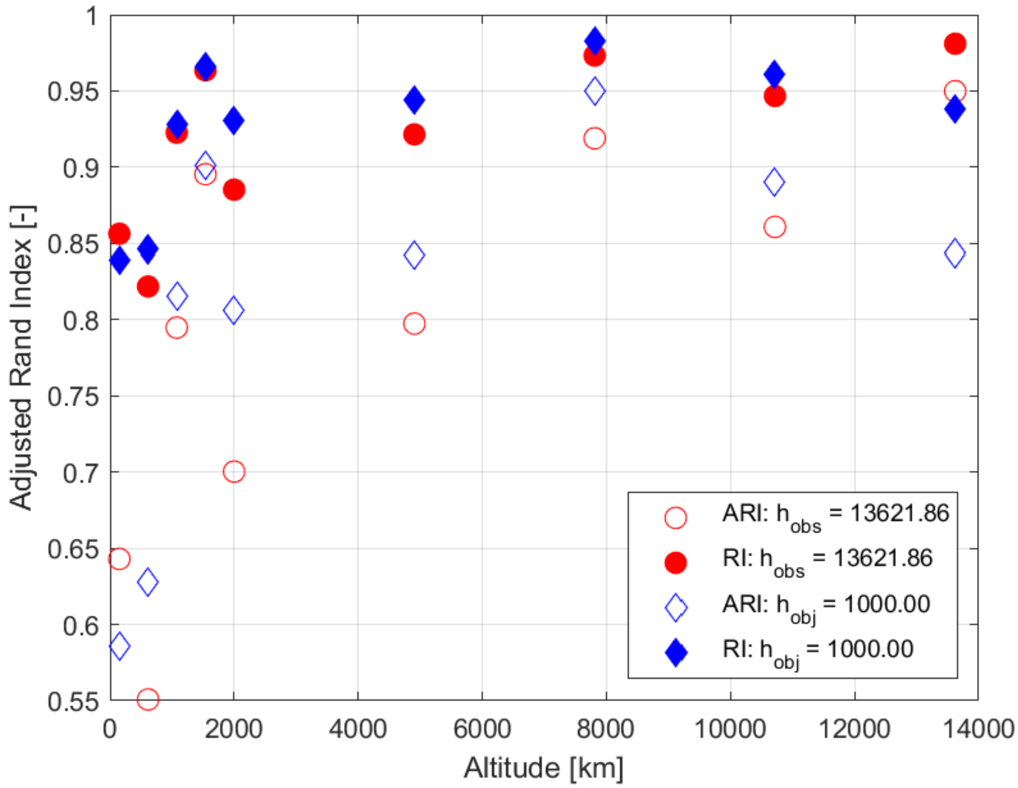

Fig. 9 Overlay of Rand Indices

Lastly, we look at the relation between the ARI, RI, and the MCR. Both metrics are plotted with respect to the MCR and a linear regression is done to aid in prediction. The data point with a MCR of 30 is treated as an outlier due to its originating from the test-point that encountered errors during computation. Equations for the linear regression lines are presented in Equations 24 and 25.

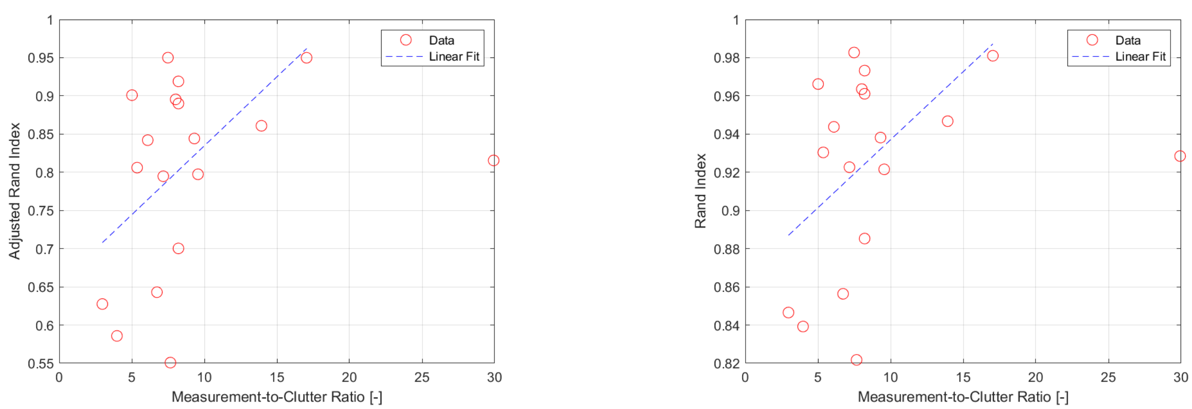

(a) Adjusted Rand Index **(b) Rand Index**

Fig. 10 Rand vs. MCR

$$R = 0.0071 * MCR + 0.8658 \tag{24}$$

$$R_A = 0.0181 * MCR + 0.6541 \tag{25}$$

Both equations are rearranged to calculate predicted MCR values for a given RI or ARI. These predictions are tabulated in Table 2 utilizing four common rules-of-thumb for Rand index evaluation: $R \geq 90$ corresponds to excellent recovery, $90 > R \geq 80$ is good recovery, $80 > R \geq 65$ is moderate recovery, and $R < 0.65$ is poor recovery. In this context, recovery refers to the algorithms ability to recover the true labels of each measurement.

$$MCR = \frac{R - 0.8658}{0.0071} \tag{26}$$

$$MCR = \frac{R_A - 0.6541}{0.0181} \tag{27}$$

Desired RI (%)	Minimum MCR	Desired ARI (%)	Minimum MCR
100	18.8393	100	19.1105
90	4.8008	90	13.5856
80	-9.2378	80	8.0608
65	-30.2956	65	-0.2290

Table 2 MCR Thresholds to Single-Stage EM Predicted Performance

V. Discussion

The results paint a picture of the dependence of single-stage EM algorithm on observer altitude. Focusing strictly on classification performance based on assumptions outlined in Section III.B, we see clear correlation between altitude and the different formulations of the Rand index 9. This is also made evident with the mixing proportion error, Figure 7b, in quantifying the amount of miss-classification at each of the test points. Moving from point to point these trends do not necessarily hold, but this is believed to be a result of insufficient sampling and is discussed in Section VI.

The correlation between these two parameters is insufficient to claim a cause, but reviewing the measurement properties in Figure 5 allows us to draw further conclusions. Looking at the data we see the MCR, 5a grows as a function of altitude.Based on Equation 10, for its value to increase the number of object measurements must increase or the number of clutter measurements must decrease. Our knowledge of the clutter model tells us that there is no direct way to increase the former but the latter could be decreased if the probability of occlusion for a given object was reduced.

The other property calculated directly from the measurements, density, does not provide the same clear conclusions. Looking at equation 11, we see for the density to increase, either the number of non-clutter measurements must increase, or the solid angle that contains all non-clutter measurements must decrease. The latter is a function of the elevation range of the measurements which we see varies based on altitude in Figure 3. The former, similar to, MCR is a function of the probability of occlusion. A higher probability of occlusion will increase the number of non-clutter measurements and in-turn increase measurement density. Applying this understanding of the phenomena to the values of density observed in Figure 5b, with a low-altitude observer, the density grows with altitude supporting the argument that density can serve as a performance predictor. When looking at the high-altitude case, this same trend is not existent. This is likely due to the factor of the solid angle. Although it is shown to vary with altitude, its evolution was not fully quantified in this study. Although an interesting metric to track in future work, the predictive power of the MCR was the focus of this study moving forward.

Before continuing our evaluation of performance, we must first resolve the discrepancy between the two variations of the Rand index. Both metrics quantify the classification accuracy, but the two formulations make different assumptions on the possible variability in the labels. The ARI assumes that the number of labels is not a fixed quantity and adjusts the score for possible permutations in the number of labels and the quantity of measurements distributed among them. With a fixed quantity of possible object orbits and clutter, this causes the ARI to overly penalize the score. For this reason, in the single-stage formulation, the standard Rand index is a better measure of classification performance than the adjusted Rand index. In future work with the multi-stage formulation, the ARI will be a powerful tool. This is due to the multi-stage formulations ability to predict the number of orbits to fit rather than requiring that information to be provided.

Treating the Rand index as our primary classification metrics we review the tabulated MCR thresholds for algorithm performance. Since a negative MCR implies that the quantity of object measurements or clutter measurements is negative, the implication of this first order model is that the qualitative recovery of the labels will always be either "good" or "excellent". This may be true for the simplified version of the algorithm implemented here, but is unlikely broadly true to the EM methodology. Improvements to model fidelity, as discussed in Section VI, and an increased understanding of the algorithm overall will allow this performance model to be refined to more correctly predict the expected Rand index given the MCR.

The final point to discuss is the MCR itself. The MCR is not a quantity that would be known in an operational environment to help predict performance. However, in this study it serves as an analogue for a quantity that can be derived as a function of expected object and observer orbits, the probability of occlusion. Deriving this quantity will allow for one to quantify the expected performance of the algorithm given some set of objects or general orbital regions.

VI. Future Work

In order to fully develop this technique for autonomous measurement association and orbital determination several further iterations are required. These advancements will resolve questions in several areas of the algorithm. These areas are listed below.

1) Sampling
2) Higher-Order Dynamics
3) Observability/Sensor Modeling
4) Object Maneuvers

A. Sampling

The experiments performed during this study were done with a limited sample size of 18 test points and 10 runs per point. This resolution is insufficient to fully characterize the affects of altitude on the algorithm. Although sufficient for first order predictions, a greater number of test points would help reduce the affects of outliers on the data. Similarly a greater number of runs per point would help reduce the uncertainty in those mean values and improve overall prediction quality.

B. Dynamics

The two body problem is insufficient to precisely determine the orbit of an object [19]. Perturbations from various sources affect the orbit and add complexity to the EM algorithm by requiring numerical integration of the orbital state. Two major perturbations should be studied to further build confidence in the EM methodology.

Atmospheric drag plays a major role in orbit evolution, especially for objects in the LEO regime where the methodology exhibited performance degradation. Simple models exist to represent Earth's atmosphere. Models such as the exponential atmosphere could be implemented quickly to increase overall accuracy with minimal impact on computation complexity [19]. More complex models can also be implemented such as Jacchia-Roberts [24] or Jacchia-Bowman [25]. These models would improve fidelity, especially, in LEO, but at the cost of computation time and algorithm complexity. Both of these models require tracking of additional parameters that would have to be assumed known or estimated in some fashion.

Although a good first approximation, a spherical Earth does not accurately represent the gravitational forces exhibited on objects in orbit. The original author showed good results with the inclusion of the oblateness perturbation (J2). Although a step in the right direction, higher order gravity terms would be ideal to completely validate this methodology and quantify its potential in estimation and classification. Spherical harmonics provides a vector for implementing this type of model [19]. The optimal degree and order for this model would have to be determined as a trade between computational complexity and model accuracy. Even so, a modest degree and order would still constitute an improvement over the most complex gravitation model used to date with the EM methodology.

Other perturbations could be studied with this methodology. Effects such as lunar perturbations and solar radiation pressure would have a non-zero impact on state evolution [19]. Compared to the aforementioned techniques however, their impact would be of a much smaller order of magnitude that may not warrant the additional computational complexity for this problem.

C. Observability/Sensor Modeling

In this section, observability is defined as the ability of the observers sensor(s) to measure the desired objects. In the original reference, and in this paper, there was no maximum range, azimuth, or elevation that was imposed on the sensor. Although an unconstrained azimuth is possible with a satellite capable of body axis rotation, most optical sensors have some elevation constraint as well as practical range limitations [26]. These restrictions impose limits on the observer-object geometries that produce valid measurements instead of clutter. Based on the observed dependence on MCR to produce good performance, a realistic sensor model could reveal additional shortcomings in the methodology. A similar impact would be seen from the measurement rates. These are unlikely to be at the constant rate of 1 measurement per 10 minutes as used here and in the original work. Both of these enhancements, would alter the number and mixing proportion of measurements depending on the geometry of the problem. As this algorithm has so far only been tested with stable geometries and constant measurement rates, this would be a key area to continue testing to verify that different time-series of data did not cause adverse effects.

D. Object Maneuvers

It is often necessary for satellites, especially members of constellations, to adjust their orbits for collision avoidance and general station keeping [1, 2]. These types of maneuvers would introduce a step to the observations that could prove challenging to associate to an orbit model. The algorithm could fail to converge or converge to an average state that is not representative of either the initial or the final orbit. This type of phenomena could prove a significant limitation to this algorithm, however methods to inject known maneuvers could be inserted into the estimation scheme. The affect of, and any possible mitigation to, object maneuvers needs to be further studied to support the use of this technique in operational environments.

VII. Conclusion

The single-stage EM algorithm, developed by Bernstein, was recreated in an effort to quantify the impacts of various observer and object altitudes on algorithm predictive ability. Of interest was the correct prediction of the initial orbital state to a sufficiently small level of position and velocity error. Additionally, the measurement concentration estimate and the data association metrics are of interest as orbits were varied between 1000km and 13622 km altitude. Validation was conducted to ensure that performance was in line with what was achieved by Bernstein. This validation yielded mixed results. The algorithm did not display the same ability to estimate position, velocity, and concentration compared to the results of the original author. However, it's ability to correctly classify and associate measurements met the performance criteria.

Assuming high classification performance will be maintained as the algorithm implementation is refined, the performance was analyzed for a set of 19 test points consisting of various observer and object altitudes. Data showed that classification performance, as quantified by the ARI and RI, had a positive correlation with both object and observer altitude. As objects were placed higher and higher the ability of the algorithm to converge to a near-truth association increased. Although not fully validated, the estimates of other parameters showed similar trends where smaller errors were correlated with higher altitudes. This type of correlation to altitude is not unexpected for such an algorithm as the relative dynamics between the observer and the objects will be impacted by the difference in altitude.

In addition to altitude in general, the measurement-to-clutter ratio was quantified at each altitude. This metric showed a strong positive correlation to altitude. Based on this metric a first order model was derived, through linear regression, to predict the RI and ARI as functions of the MCR. Given the dependence on MCR, techniques to minimize the sampling of clutter could be studied. If the algorithm's performance is more so related to the MCR rather than altitude directly, then these techniques would allow performance in the low-altitude region to be improved and the number of feasible observer configurations expanded.

Without such techniques, the data implies that taking measurements from an observer to objects at lower altitudes poses some risk. Consistent measurements from orbits lower than 1000 km would begin to impact the single-stage EM scheme as those orbits posses lower estimation and classification performance. The proportion of measurements originating from the high-altitude region, to that in the low-altitude region required to maintain performance was not derived as part of this study. However, this value would be important to quantify in follow-on work. It would help further refine the known constraints of the algorithm. Additionally, the multi-stage EM approach could provide benefits in a mixed altitude scenario, but was not implemented as part of this study.

In general, this EM algorithm and its extensions remain an interesting area of development for multi-object tracking. The methodology requires additional maturation and generalization to account for various types of orbits as well as the behaviors of the object in those orbits. Investigation of this technique should be continued to explore greater complexity and to quantify any remaining uncertainty in performance.

References

[1] Lal, B., Balakrishnan, A., Caldwell, B. M., Buenconsejo, R. S., and Carioscia, S. A., "Global Trends in Space Situational Awareness (SSA) and Space Traffic Management (STM)," Tech. Rep. D-9074, Institute for Defense Analyses, Washington D.C., Apr. 2018.

[2] Oltrogge, D. L., and Alfano, S., "The technical challenges of better Space Situational Awareness and Space Traffic Management," Journal of Space Safety Engineering, Vol. 6, No. 2, 2019, pp. 72–79. https://doi.org/https://doi.org/10.1016/j.jsse.2019.05.004, URL https://www.sciencedirect.com/science/article/pii/S2468896719300333, space Traffic Management and Space Situational Awareness.

[3] Klinkrad, H., Space Debris: Models and Risk Analysis, Springer Praxis Books, Springer Berlin Heidelberg, 2006.

[4] Jones, B. A., Bryant, D. S., Vo, B.-T., and Vo, B.-N., "Challenges of multi-target tracking for space situational awareness," 2015 18th International Conference on Information Fusion (Fusion), 2015, pp. 1278–1285.

[5] Dempster, A. P., Laird, N. M., and Rubin, D. B., "Maximum Likelihood from Incomplete Data via the EM Algorithm," Journal of the Royal Statistical Society. Series B (Methodological), Vol. 39, No. 1, 1977, pp. 1–38. URL http://www.jstor.org/stable/2984875.

[6] Davey, S. J., Bessell, T., Cheung, B., and Rutten, M., "Track before Detect for Space Situation Awareness," 2015 International Conference on Digital Image Computing: Techniques and Applications (DICTA), 2015, pp. 1–7. https://doi.org/10.1109/DICTA.2015.7371316.

[7] Xin, W., "Orbit Determination of Mixed Observations of Multiple Objects1, 2," Chinese Astronomy and Astrophysics, Vol. 39, No. 2, 2015, pp. 254–264. https://doi.org/https://doi.org/10.1016/j.chinastron.2015.04.011, URL https://www.sciencedirect.com/science/article/pii/S0275106215000399.

[8] Cheung, B., Rutten, M., Davey, S., and Cohen, G., "Probabilistic Multi Hypothesis Tracker for an Event Based Sensor," 2018 21st International Conference on Information Fusion (FUSION), 2018, pp. 1–8. https://doi.org/10.23919/ICIF.2018.8455718.

[9] Kent, J. T., Bhattacharjee, S., Hussein, I. I., Faber, W. R., and Jah, M., "Fisher-Bingham-Kent Mixture Models for Angles-Only Observation Processing," 2018 Space Flight Mechanics Meeting, 2018. https://doi.org/10.2514/6.2018-1972, URL https://arc.aiaa.org/doi/abs/10.2514/6.2018-1972.

[10] Siminski, J., and Jilete, B., "Resolution of track association ambiguities using expectation-maximization algorithm," 1st NEO and Debris Detection Conference, 2019.

[11] Bernstein, J., "Probabilistic Data Association for Orbital-Element Estimation Using Multistage Expectation–Maximization," Journal of Aerospace Information Systems, Vol. 18, No. 5, 2021. https://doi.org/10.2514/1.i010826, URL https://www.osti.gov/biblio/1772302.

[12] Bishop, C. M., Pattern Recognition and Machine Learning (Information Science and Statistics), Springer-Verlag, Berlin, Heidelberg, 2006.

[13] Rand, W. M., "Objective Criteria for the Evaluation of Clustering Methods," Journal of the American Statistical Association, Vol. 66, No. 336, 1971, pp. 846–850. https://doi.org/10.1080/01621459.1971.10482356, URL https://www.tandfonline.com/doi/abs/10.1080/01621459.1971.10482356.

[14] Vinh, N. X., Epps, J., and Bailey, J., "Information Theoretic Measures for Clusterings Comparison: Is a Correction for Chance Necessary?" Proceedings of the 26th Annual International Conference on Machine Learning, Association for Computing Machinery, New York, NY, USA, 2009, p. 1073–1080. https://doi.org/10.1145/1553374.1553511, URL https://doi.org/10.1145/1553374.1553511.

[15] Lauritzen, S. L., "Lectures on Contingency Tables," , October 2002.

[16] Schroeder, D., and Inc, E. I., Astronomical Optics, Electronics & Electrical, Elsevier Science, 2000.

[17] Mazonka, O., "Solid Angle of Conical Surfaces, Polyhedral Cones, and Intersecting Spherical Caps," , 2012. https://doi.org/10.48550/ARXIV.1205.1396, URL https://arxiv.org/abs/1205.1396.

[18] Hauberg, S., "Directional Statistics with the Spherical Normal Distribution," 2018 21st International Conference on Information Fusion (FUSION), 2018, pp. 704–711. https://doi.org/10.23919/ICIF.2018.8455242.

[19] McClain, W., and Vallado, D., Fundamentals of Astrodynamics and Applications, Space Technology Library, Springer Netherlands, 2001.

[20] Süli, E., and Mayers, D. F., An Introduction to Numerical Analysis, Cambridge University Press, 2003. https://doi.org/10.1017/CBO9780511801181.

[21] Broucke, R. A., and Cefola, P. J., "On the Equinoctial Orbit Elements," Celestial Mechanics, Vol. 5, No. 3, 1972, pp. 303–310. https://doi.org/10.1007/BF01228432.

[22] Moré, J. J., "The Levenberg-Marquardt algorithm: Implementation and theory," Numerical Analysis, edited by G. A. Watson, Springer Berlin Heidelberg, Berlin, Heidelberg, 1978, pp. 105–116.

[23] Nocedal, J., and Wright, S. J. (eds.), Quasi-Newton Methods, Springer New York, New York, NY, 1999, pp. 192–221. https://doi.org/10.1007/0-387-22742-3_8, URL https://doi.org/10.1007/0-387-22742-3_8.

[24] Roberts, J., Charles E., "An Analytic Model for Upper Atmosphere Densities Based Upon Jacchia's 1970 Models," Celestial Mechanics, Vol. 4, No. 3-4, 1971, pp. 368–377. https://doi.org/10.1007/BF01231398.

[25] Bowman, B., Tobiska, W. K., Marcos, F., Huang, C., Lin, C., and Burke, W., A New Empirical Thermospheric Density Model JB2008 Using New Solar and Geomagnetic Indices, 2012. https://doi.org/10.2514/6.2008-6438, URL https://arc.aiaa.org/doi/abs/10.2514/6.2008-6438.

[26] Hampf, D., Wagner, P., and Riede, W., "Optical technologies for the observation of low Earth orbit objects," , 2015. https://doi.org/10.48550/ARXIV.1501.05736, URL https://arxiv.org/abs/1501.05736.